

Eric T. DeShong¹

Pennsylvania State University,
3127 Research Drive,
State College, PA 16801
e-mail: etd5060@psu.edu

Benjamin Peters

Georgia Institute of Technology,
Groschlose 320,
Atlanta, GA 30332
e-mail: bpeters9@gatech.edu

Reid A. Berdanier

Pennsylvania State University,
3127 Research Drive,
State College, PA 16801
e-mail: rberdanier@psu.edu

Karen A. Thole

Pennsylvania State University,
3127 Research Drive,
State College, PA 16801
e-mail: kthole@engr.psu.edu

Kamran Paynabar

Georgia Institute of Technology,
Groschlose 320,
Atlanta, GA 30332
e-mail: kamran.paynabar@isye.gatech.edu

Nagi Gebraeel

Georgia Institute of Technology,
Groschlose 320,
Atlanta, GA 30332
e-mail: nagi.gebraeel@isye.gatech.edu

Correlating Time-Resolved Pressure Measurements With Rim Sealing Effectiveness for Real-Time Turbine Health Monitoring

Purge flow is bled from the upstream compressor and supplied to the under-platform region to prevent hot main gas path ingress that damages vulnerable under-platform hardware components. A majority of turbine rim seal research has sought to identify methods of improving sealing technologies and understanding the physical mechanisms that drive ingress. While these studies directly support the design and analysis of advanced rim seal geometries and purge flow systems, the studies are limited in their applicability to real-time monitoring required for condition-based operation and maintenance. As operational hours increase for in-service engines, this lack of rim seal performance feedback results in progressive degradation of sealing effectiveness, thereby leading to reduced hardware life. To address this need for rim seal performance monitoring, this study utilizes measurements from a one-stage turbine research facility operating with true-scale engine hardware at engine-relevant conditions. Time-resolved pressure measurements collected from the rim seal region are regressed with sealing effectiveness through the use of common machine learning techniques to provide real-time feedback of sealing effectiveness. Two modeling approaches are presented that use a single sensor to predict sealing effectiveness accurately over a range of two turbine operating conditions. Results show that an initial purely data-driven model can be further improved using domain knowledge of relevant turbine operations, which yields sealing effectiveness predictions within 3% of measured values. [DOI: 10.1115/1.4053175]

Keywords: fluid dynamics and heat transfer phenomena in compressor and turbine components of gas turbine engines, measurement techniques

Introduction

The pursuit of highly efficient gas turbine engines demands high temperatures at the turbine inlet to improve thermodynamic efficiency. However, these high temperatures present a durability risk to the engine because the main gas path (MGP) temperature exceeds the hardware material softening temperature [1]. Internal and external cooling strategies have been developed for MGP components, but under-platform hardware components require a different strategy to maintain acceptable material temperatures. To prevent ingestion into the under-platform region and protect turbine components, highly engineered rim seal geometries and purge flows are typically employed.

Due to the complex fluid dynamics associated with rim seal ingestion and cavity flows, the majority of research into rim sealing performance has focused on understanding the flow physics with a goal to improve the design of seal geometries and purge flow injection configurations. This type of research applies to the initial design and performance characterization of rim seals, which does not cover the entire rim seal life cycle. Once a rim seal and purge flow injection design has been commissioned into an engine, there is very little research available to inform the

real-time health monitoring of rim sealing performance during operation.

In their review of condition-based maintenance of gas turbines, Tahan et al. [2] identified turbine and compressor component faults as most important due to their critical influence on engine performance and their expense relative to other engine components. This statement highlights the importance of monitoring rim seal performance because poor sealing effectiveness results in damage to both rotating and stationary turbine components. Tahan et al. also classified cooling and sealing faults as an auxiliary subsystem fault, which is most readily identified using nonperformance-based identification methods. This type of identification is distinct from the gas path analysis [3], which monitors engine performance metrics like efficiency and power.

Based on these assessments, a fault identification methodology specifically tailored to rim seal performance is necessary to prevent costly engine failures. This unique study addresses this need by presenting two data-driven (DD) modeling approaches that use a single-pressure sensor to predict the sealing effectiveness in real time.

The remaining structure of this article will be laid out as follows. First, literature relevant to the quantification of rim sealing effectiveness in an engine environment will be reviewed, followed by a description of the experimental methods that were employed. Then, a brief explanation of the unsteady rim flow characteristics will be given to setup the discussion of the two modelling approaches. Each modeling approach will be explained in detail, followed by a discussion of the practical considerations necessary

¹Corresponding author.

Contributed by the International Gas Turbine Institute (IGTI) of ASME for publication in the JOURNAL OF TURBOMACHINERY. Manuscript received August 12, 2021; final manuscript received November 24, 2021; published online January 28, 2022. Assoc. Editor: Randall M. Mathison.

for the implementation of the models in a realistic engine application. Finally, the results and conclusions will be discussed.

Literature Review

The majority of rim seal studies have focused on developing a physical understanding of the mechanisms that drive ingestion. In a comprehensive review, Johnson et al. [4] summarized the physical mechanisms of rim seal ingestion: disk pumping, vane and blade pressure field interaction, 3D rim seal geometry, rim seal geometry asymmetries, turbulent transport, and flow entrainment. More recently, Scobie et al. [5] further summarized the driving factors for ingestion as externally induced (EI), rotationally induced (RI), or combined ingress (CI), which is a combination of EI and RI ingress.

This physical understanding of rim seal ingestion mechanisms has largely relied on the measurement of sealing effectiveness for a variety of experimental setups and flow conditions. The most widely utilized method for quantifying sealing effectiveness is the gas concentration method [6–8], which uses a tracer gas, typically CO₂, to differentiate purge flow and MGP flow that has entered the under-platform region. By using this approach, the sealing effectiveness is measured at multiple purge flowrates to quantify the relationship between the two parameters. Using experimental results and an understanding of rim seal ingestion mechanisms, researchers have created physics-based models to define a functional relationship between the sealing effectiveness and the purge flowrate [9–11]. Because these physics-based models require only a few inputs to model the sealing performance, they can be potentially applied to the real-time monitoring of sealing effectiveness.

Of course, the application of temperature measurements on the under-platform hardware would be the most direct method for quantifying ingestion. This is feasible when ingestion occurs along the stationary side of the rim seal hardware, as shown in the study by Scobie et al. [5]. However, multiple researchers have also shown that ingestion can occur along the rotating side of the rim seal [12–15]. Such a flow scenario could cause a stator-side temperature sensor to measure hardware temperature driven by egressing cooler flow rather than ingested hot main gas path flow. This scenario obfuscates the relationship between stator hardware temperature and sealing effectiveness, which diminishes the robustness of using a temperature sensor to quantify ingestion in a realistic engine environment.

Many researchers have presented orifice models to derive a mathematical relationship between sealing flowrate and ingestion [16–19]. Owen recently presented a model, which simplified the rim seal to an orifice ring with separate ports for ingress and egress, and derived a set of equations commonly referred to as the “orifice equations.” These equations were defined for RI [9] ingress, as well as EI and CI types of ingress [10]. On the basis of these equations, Sangan et al. derived the “effectiveness equations” [8,20]. Critically, these equations have two unknowns, the ratio of discharge coefficients and the minimum nondimensional sealing parameter, that must be determined experimentally.

By using these equations, Owen et al. [21] developed a method to relate engine pressure measurements to the sealing effectiveness. The instrumentation requirements for this method are relatively simple; however, implementation requires some key assumptions and extensive simulation and experimental work.

Specifically, a seal design must be tested in an experimental facility to determine the ratio of discharge coefficients and gather pressure measurements in the annulus and wheel-space regions. This ratio of discharge coefficients is assumed to be constant between rig and engine conditions. Then, unsteady computational fluid dynamics (CFD) must be performed to determine the precise axial and circumferential locations (referred to as the “sweet spot”) at which pressure measurements should be gathered in the engine. The orifice equations relate the pressure measurements at this location and the experimentally determined ratio of discharge coefficients to the sealing effectiveness in the engine. To compute

the sealing flowrate, the pressure measurements from the rig must be corrected to the sweet spot location to determine the discharge coefficient for egress. A further correction must be applied to the pressure coefficient to account for the Mach number ratio between the experimental facility and the engine [22]. Together, these experimental, computational, and analytical efforts enable the calculation of the sealing effectiveness.

Scobie et al. [5] showed good agreement between the orifice model and experimental data gathered from a variety of test turbines with differing rim seal geometries, operating environments, and driving ingestion mechanisms. However, these experimental data ubiquitously show a smoothly increasing trend that does not exhibit regions of inflection. While this relationship between sealing effectiveness and purge flowrate is observed in many scenarios, there are also many studies that have shown significant inflection regions [14,23–29]. Hence, the orifice model lacks widespread applicability to all turbine geometries.

Overall, creating a generalized physics-based model that captures the inflection region is not currently feasible because the flow physics that drive the inflection are not well understood. To address this issue, the present study utilizes a data-driven modeling approach to relate time-resolved pressure data to the sealing effectiveness measured in an experimental facility. Results show that this modeling approach is viable, even in the presence of a sealing effectiveness curve inflection. In addition, the data-driven modeling approach is relatively simple in its implementation because it does not require computational flow simulation. These characteristics highlight the opportunity for a data-driven model to be applied as a preferred method for real-time rim seal performance monitoring of in-service engines.

Experimental Setup and Testing Procedure

This study was performed at the Steady Thermal Aero Research Turbine (START) facility at Penn State University [30,31]. The facility layout is shown in Fig. 1, with arrows highlighting the various flow paths.

The START facility operates in a continuous-duration mode to emulate the steady operation of a gas turbine engine. The flow path is open loop and begins with two industrial compressors that intake ambient air with a maximum flow capability of 11.4 kg/s (25 lb_m/s) at 480 kPa (70 psia). This process raises the fluid temperature to approximately 380 K (230 °F) at the compressor exit depending on ambient temperature conditions. Next, the compressor exit flow is split between two distinct flow paths. The majority of the flow proceeds through an in-line natural gas heater chamber that provides the high-temperature MGP flow. The maximum capability of the heater is 675 K (750 °F) at nominal flowrate conditions. The remainder of the compressor exit flow is diverted through a heat exchanger to lower its temperature to about 273 K (32 °F). This fluid stream is further separated into multiple independently metered coolant flows, which are distributed throughout the turbine.

These MGP and coolant flows ultimately reconvene in the test section, which consists of a one-stage axial turbine comprising hardware relevant to the current state-of-the-art for turbine design. A cross-sectional view of the test article showing qualitatively equivalent geometry representative of the actual START test section hardware is shown in Fig. 2.

The purge flow pressure and temperature were measured beneath the vane, just before the purge flow injection to the rim seal and under-platform regions. Although the START facility is capable of supplying the test section with multiple coolant streams, the purge flow was the sole coolant stream flowing in this experiment. The MGP and purge flowrates were measured individually upstream of the test section using Venturi flowmeters. In total, nine purge flow conditions were used for this study, and the purge flowrate (\dot{m}_p) was normalized by the maximum purge flowrate required to fully seal the rim cavity at sensor $P_A(\dot{m}_{p,\min,A})$.

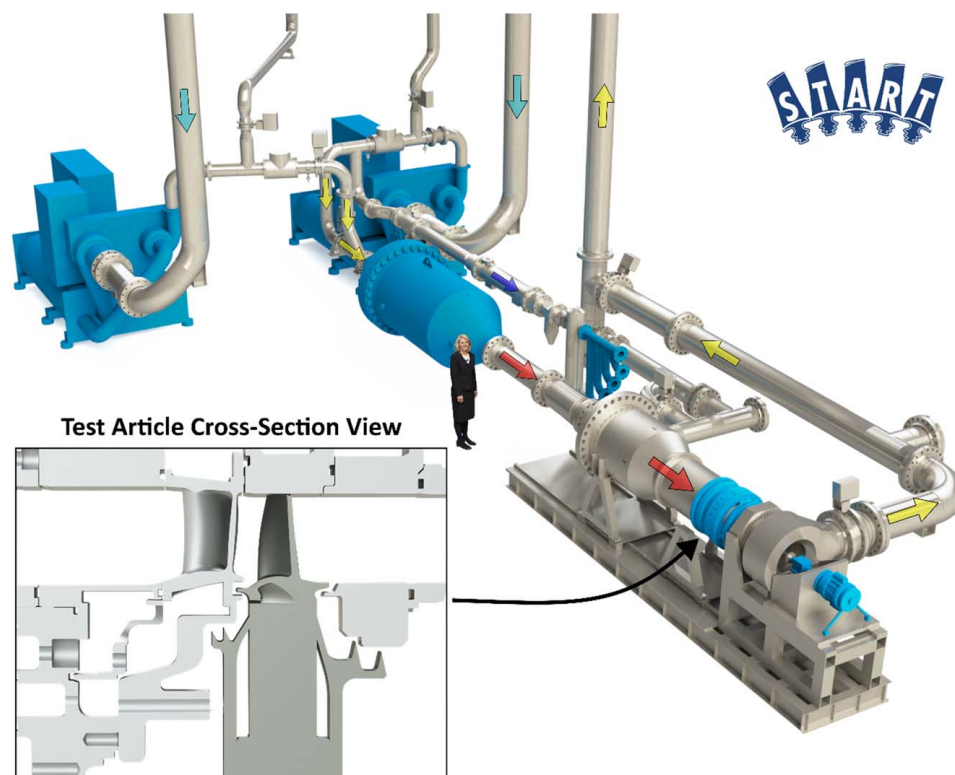


Fig. 1 START facility layout with major components highlighted and arrows indicating the direction of fluid flow

This experiment leveraged an additively manufactured vane with design features and internal wire routing passages to accommodate fast-response piezoresistive pressure transducer installations. These fast-response sensors are labeled P_A and P_G in Fig. 2. Signals were sampled at a nondimensional frequency of $f_s/f_D \approx 600$, where f_D represents the disk rotational frequency, with analog low-pass filtering to prevent aliasing. The nondimensional resonant frequency of the sensors is represented by at least $f/f_D \approx 120$, which provides a usable bandwidth that far exceeds the range of interest for this study. The calibration of the sensors is given by Siroka et al. [32].

Measurements from these sensors were collected over 500 revolutions at nine purge flowrates, with nine data sets collected at each purge flowrate to facilitate model training and testing procedures. Although not shown here, a separate analysis showed 100 revolutions was a critical value below which model accuracy decreased substantially. Between 100 and 500 revolutions, there were slight improvements to model performance with increased revolution count, but it is assumed that including additional data beyond 500

revolutions would offer negligible benefits to the predictive model accuracy.

The gas concentration-based sealing effectiveness was used in this study to quantify the rim sealing performance. The sealing effectiveness is calculated according to Eq. (1):

$$\varepsilon = \frac{c_A - c_{MGP}}{c_P - c_{MGP}} \quad (1)$$

which relates CO_2 concentration measurements to the sealing effectiveness. The concentration sampling locations are labeled in Fig. 2. The uncertainties of these pressure, temperature, mass flowrate, speed, and sealing effectiveness measurements are presented in Table 1. Prime notation indicates a value that is nondimensionalized by the nominal operating condition (OP1). These uncertainties were computed according to the procedure outlined by Figliola and Beasley [33].

Unsteady Rim Flow Characteristics

As the purge flow injected into the under-platform region is varied, the characteristics of the unsteady flow field change as

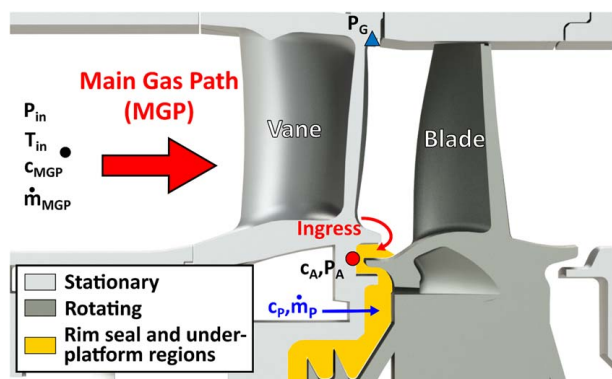


Fig. 2 Cross-section view of one-stage turbine test article showing flow configuration instrumentation locations

Table 1 Measurement uncertainties

Parameters	Total uncertainty
Main gas path flowrate, $(\dot{m}_{MGP})'$	± 0.007
Shaft rotational speed, RPM'	± 0.001
Inlet pressure, P'_{in}	± 0.002
Inlet temperature, T'_{in}	± 0.001
1.0 stage pressure ratio, $(P_{in}/P_{out})'$	± 0.01
Sealing effectiveness, ε	± 0.015 to ± 0.025
Fast-response pressures, P^* [32]	± 0.00005
Normalized purge flowrate, $\frac{\dot{m}_P}{\dot{m}_{P, \min, A}}$	± 0.018

well. Monge-Concepción et al. [34] provide a detailed investigation of the unsteady fluid mechanics in the under-platform region measured at the START facility, and Siroka et al. [32] describe how the dominant unsteady flow features affect ingestion. Because the present study relies upon modeling the relationship between the time-resolved pressure signals and the sealing effectiveness, it is important to first understand the unsteady characteristics of the rim cavity flow. These topics are briefly summarized here, and readers are directed to referenced studies for further details.

The variation of sealing effectiveness at location A with normalized purge flowrate is shown in Fig. 3(a). There is an inflection in the sealing effectiveness curve that appears at approximately half the purge flowrate required to fully seal rim cavity location A.

The time-resolved pressure was measured throughout the range of purge flowrates using fast-response pressure sensors at locations A and G. A fast Fourier transform (FFT) was applied to these pressure signals to create frequency spectra from the time-domain signals. The pressure amplitude was normalized for presentation in this article according to Eq. (2):

$$P^* = \frac{P - P_{\min}}{P_{\max} - P_{\min}} \quad (2)$$

where P_{\max} and P_{\min} represent the maximum and minimum pressure amplitude across all purge flowrates and sensors. The frequency domain was nondimensionalized with respect to the disk rotating speed.

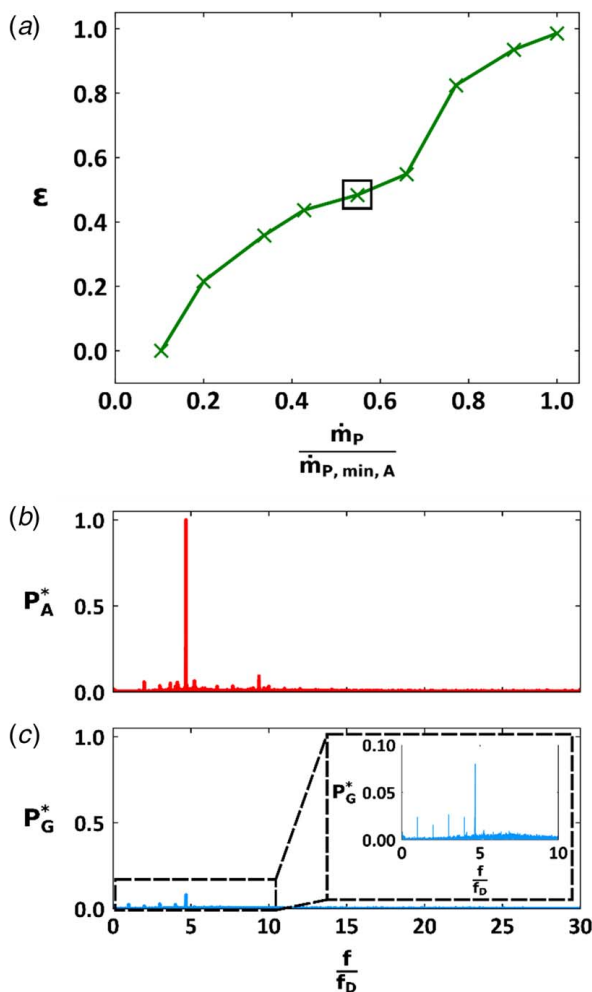


Fig. 3 Measured (a) sealing effectiveness versus purge flowrate at location A and frequency spectra from pressure sensors, (b) P_A , and (c) P_G . The box in (a) identifies the condition corresponding to the frequency spectra in (b) and (c).

The frequency spectra from fast-response pressure sensors A and G are shown in Figs. 3(b) and 3(c) for the normalized purge flowrate corresponding to the maximum unsteadiness. The time-domain pressure signal was digitally filtered at a cutoff frequency of $f/f_D = 30$ to remove the blade passing frequency, so none of the peaks in the frequency domain correspond to blade passing events. Figure 3(b) shows a dominant frequency at approximately five times the disk rotating frequency ($f/f_D \approx 5$). This dominant frequency is created by rotating flow structures, as described in detail by Monge-Concepción et al. [34], and similar behaviors have been identified by a broad community of researchers using both experimental and numerical methods [11,13–15,24–27,32,34–55].

Notably, the pressure fluctuations from these rotating flow structures propagate radially outward through the MGP and are measured at the outer casing wall by pressure sensor P_G . The pressure fluctuations are significantly attenuated as they propagate to the casing, which decreases the pressure amplitude to about 8% of the pressure amplitude measured in the rim seal. While this attenuation is suboptimal for measuring rim seal pressure fluctuations at the casing, location G is likely a more accessible position for sensor installation than location A.

The amplitude of the dominant frequency at location A is shown as a function of purge flowrate alongside the sealing effectiveness curve in Fig. 4. As the purge flowrate increases toward a normalized value of about 0.55, the strength of the rotating flow structures (indicated by the amplitude of the dominant frequency component) also increases. As the flow structures associated with the identified frequency content form and strengthen, they drive additional ingestion, which subsequently creates the inflection in the sealing effectiveness measurements [32]. For normalized purge flowrates greater than 0.55, the flow structures begin to weaken and dissipate, which results in an associated increase of sealing effectiveness. The relationship presented in Fig. 4 forms the foundation through which the time-resolved pressure data are related to the sealing effectiveness in this study.

Data-Driven Model and Results

Two modeling approaches were used in this study to relate the measured time-resolved pressure to the measured sealing effectiveness. Although both approaches inherently utilize measured data to create the models, the initial modeling approach presented in this section is purely data driven (i.e., with no knowledge of the application); as a result, it is referred to herein as the DD modeling approach.

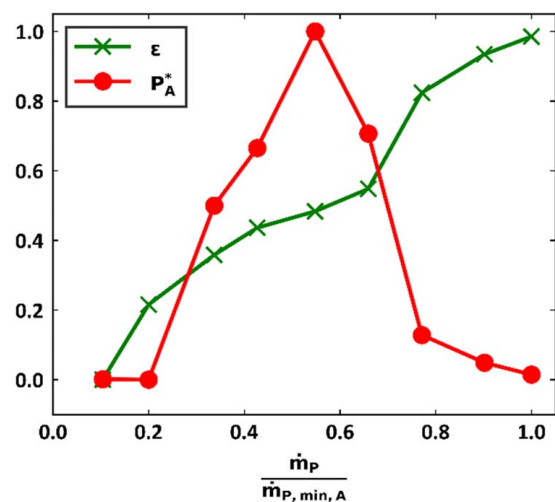


Fig. 4 Dominant frequency amplitude as a function of purge flowrate. The flow structures form and disappear as purge flow is increased to the fully sealed flowrate.

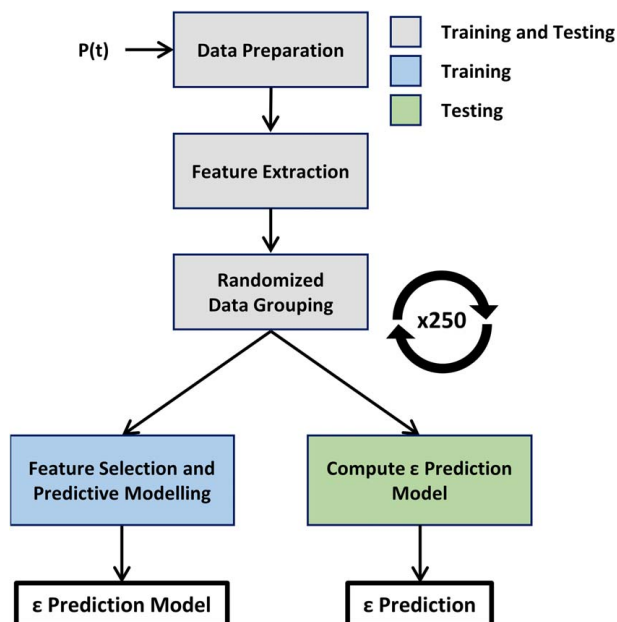


Fig. 5 Data-driven (DD) modeling diagram

The DD modeling diagram is shown in Fig. 5. This diagram outlines the steps taken to relate the input (time-resolved pressure data) to the output (the predicted sealing effectiveness). In this diagram, as well as in subsequent diagrams, the training route is always completed before the testing route. A detailed description of each modeling step is given here.

Data Preparation. The time-resolved pressure data were prepared for feature extraction by filtering and centering. As documented in previous studies [24,27,41,46,49], the frequency content of interest appears between the disk frequency and the blade passing frequency, so the filtering step reduces processing time by removing unnecessary information; this step could also be accomplished in the feature extraction step. It is expected that the cutoff frequency of the low-pass filter could be varied between the frequency content of interest and the blade passing frequency in pursuit of minor improvements to model accuracy or processing time.

The pressure data were also centered by subtracting the mean value. This centering ensured that only the fluctuations of the pressure about the mean were used in the model. The pressure data were centered to remove unnecessary information, but it is assumed that this process contributes negligibly to model accuracy and generality.

Feature Extraction. The goal of the feature extraction step was to isolate the information or quantities that would be most useful for modeling. In addition to adequately describing the pressure signal, the feature extraction also seeks to utilize a minimum amount of signal content (features) to reduce computational time. Although an exhaustive optimization process was not included in this study, three separate feature extraction techniques were investigated for comparison.

Due to the fast-response nature of the pressure sensors used in this study and the previously identified trends with specific frequency content, spectral analysis was an effective method for generating features from the time-domain pressure signal. For this reason, the three methods of feature extraction investigated were the FFT, short-time Fourier transform (STFT), and the discrete wavelet transform (DWT).

For the FFT extraction method, an averaging process was completed after the FFT was computed to reduce the number of features.

Without averaging, the total number of features is equal to the number of frequencies output from the FFT (N), which is equal to half the number of samples in the time-series pressure signal ($2N$). Due to the fast-response nature of the sensors and the high sampling rate of the data acquisition hardware used in this study, the number of pressure data points is large. If these N features are used for regression, then an $N \times N$ system of linear equations must be solved. The computational complexity of solving this system of equations scales with N^3 , so it is advantageous to characterize the signal in as few features as possible to minimize computational requirements. For this reason, frequency bins were established with a width of $f/f_D = 1$, and all spectral content within each bin was averaged. The first frequency bin extends between $0.5 \leq f/f_D < 1.5$ and the second between $1.5 \leq f/f_D < 2.5$, and this pattern was continued up to $f/f_D = 29.5$. This process effectively reduced the number of features from approximately 1.6×10^5 to 29.

For the STFT extraction method, the time domain was partitioned into 35 overlapping time intervals. Following this step, the peak amplitude, which corresponds to the large-scale rotating structures (Fig. 3(b)), was extracted from each time interval to form the feature set.

Like STFT, DWT is also able to capture time-domain variations in frequency content. However, DWT differs from STFT in that its time-frequency resolution varies when analyzing the signal at different frequencies, whereas the time-frequency resolution for the STFT is fixed upon selection of time and frequency windows. A thorough explanation of DWT and its application to fault diagnostics in gas turbines was given by Aretakis and Mathioudakis [56]. To motivate the investigation of DWT and aid in the comparison between DWT and the two Fourier transform methods, a short explanation of DWT is given here.

For a signal of length $2N$, a full wavelet decomposition breaks the signal into J sets of detail coefficients, where $J = \log_2(2N)$, and one set of approximation coefficients. Each set of detail coefficients corresponds to a specific range of frequencies, whereas the approximate coefficients represent the signal average. The DWT provides high-frequency resolution and low time resolution at low frequencies and low-frequency resolution and high time resolution at high frequencies. This characteristic of DWT is unique from STFT, which has fixed time-frequency resolution upon selection of time and frequency windows. To reduce the number of features, the sum of squares of each coefficient set was computed to represent the amount of energy in each frequency range.

After feature selection, the features from FFT, STFT, and DWT were further standardized for comparison using Eq. (3):

$$\hat{P}^* = \frac{P^* - \bar{P}^*}{\sigma_{P^*}} \quad (3)$$

where σ_{P^*} and \bar{P}^* are the standard deviation and mean of P^* , respectively.

Randomized Data Grouping. After feature extraction, the data were split into training and testing groups. As the names indicate, the model was developed using the training data and subsequently implemented for performance analysis using the testing data. Two of the nine replications at each purge flowrate were isolated for testing, while the remaining seven replications were used to train the model. Because measurements were collected at nine different purge flowrates, a total of 18 sealing effectiveness predictions were generated. To quantify prediction error, the root-mean-square error (RMSE) of each set of sealing effectiveness predictions with respect to the sealing effectiveness measurements was computed using Eq. (4):

$$\text{RMSE}(\epsilon) = \sqrt{\frac{\sum_{i=1}^n (\epsilon_{\text{pred},i} - \epsilon_{\text{meas},i})^2}{n}} \quad (4)$$

where n is equal to 18 total sealing effectiveness predictions for each data grouping iteration.

Although the data were randomly grouped, there is a potential for some data groupings to perform better or worse than others. To ensure that the grouping did not affect the interpretation of the results, the grouping, training, and testing processes were repeated 250 times. While 250 repetitions examines only a subset of all possible combinations of the data, it is assumed that 250 repetitions is sufficient to accurately capture the median RMSE(ϵ) and RMSE(ϵ) range. To investigate this assumption, the aforementioned quantities were examined for various grouping repetition counts. Results showed negligible sensitivity of median RMSE(ϵ) and RMSE(ϵ) range to additional grouping repetitions above 160 repetitions, with the maximum variation in median RMSE(ϵ) equal to 9×10^{-4} and the maximum variation in RMSE(ϵ) range equal to 2.7×10^{-3} . Therefore, 160 grouping repetitions are sufficient to capture the model performance. However, the full 250 grouping repetitions were used because additional repetitions did not add significantly to the model processing time.

Feature Selection and Prediction Modeling. After partitioning the data into training and testing groups, a subset of informative features important for predicting sealing effectiveness were selected. This process, called variable selection, is important because it separates the sparse informative features of the dataset from the noninformative features that only contribute noise. This variable selection step prevents model overfitting and improves prediction accuracy. Least absolute shrinkage and selection operator (LASSO) regression was implemented for variable selection by setting the regression coefficients of noninformative features to zero [57]. This is performed by solving the optimization problem:

$$\min_{\beta_0, \beta} \frac{1}{2n} \sum_{i=1}^n (\epsilon_i - \beta_0 - x_i^T \beta)^2 + \lambda \|\beta\|_1 \quad (5)$$

where ϵ_i is the i th sealing effectiveness of the training set, x_i is the i th set of predictors, β_0 is the intercept term, β is the vector of regression coefficients, and λ is the tuning parameter. The tuning parameter penalizes the sum of the magnitudes of the regression coefficients. Therefore, predictors that contribute noise to the model have their coefficients reduced to zero.

The tuning parameter was selected using K-fold cross-validation. The n observations are broken into K equally sized groups called folds. For a given fold, the optimization problem was solved using the other $K-1$ folds, and the associated error in predicting the sealing effectiveness was recorded. This process was then repeated for all folds, and the errors are averaged over all folds. The tuning parameter λ was then selected as a value that minimizes the average prediction error and was subsequently held constant throughout the remainder of this study.

Feature Extraction and Modeling Results. The modeling steps shown in Fig. 5 are completed for each of the three feature extraction methods (FFT, STFT, and DWT). The median and range, excluding outliers, were computed from the 250 RMSE(ϵ) quantities for each feature extraction method. Outliers were determined using the $1.5 \times \text{IQR}$ (interquartile range) rule, which dictates that any predictions $1.5 \times \text{IQR}$ above the third quartile or below the first quartile are outliers. These results are shown in Fig. 6. The bar height indicates the median RMSE(ϵ), and the range bars indicate that the range with outliers removed.

A few observations can be made from the results shown in Fig. 6. First, for these data, the FFT feature extraction method is preferred because it results in the lowest RMSE(ϵ). Furthermore, the relationship between the feature extraction methods is consistent between the two sensor locations, A and G. To further investigate these observations, the time-domain and time-frequency domain pressure signals were investigated in Fig. 7 to relate the feature extraction

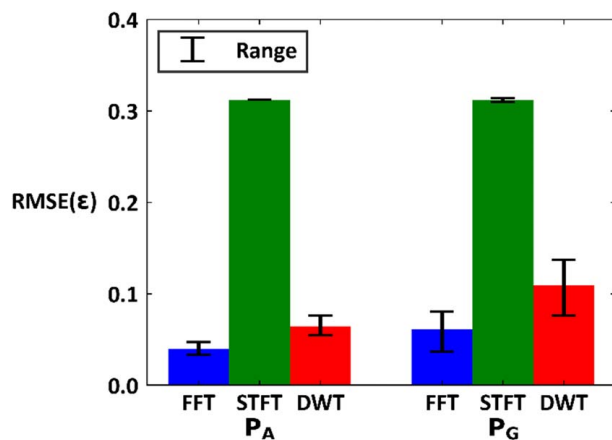


Fig. 6 Comparison of feature extraction methods based on RMSE(ϵ). These results are shown for OP1 conditions.

performance results to the physical characteristics of the pressure signal.

The time-domain pressure signal, shown in Fig. 7(a), is periodic and resembles a combination of sine waves. By definition, a wavelet is not a periodic function, which makes it ill-suited to describe the pressure signal with the aforementioned characteristics. Furthermore, the DWT and STFT are uniquely capable of representing signals that exhibit time-domain variations in the frequency content. This utility is not applicable to the pressure signals because they are stationary across many revolutions, as shown in Fig. 7(b). This stationary behavior is expected from the steady operating mode of the START facility. For these reasons, it is logical that the FFT feature extraction method results in lower prediction errors than the STFT and DWT feature extraction methods.

Referring back to Fig. 6, a general trend is observed that the RMSE(ϵ) is higher at location G than at location A. This result was expected because sensor P_A is located in the rim seal, which

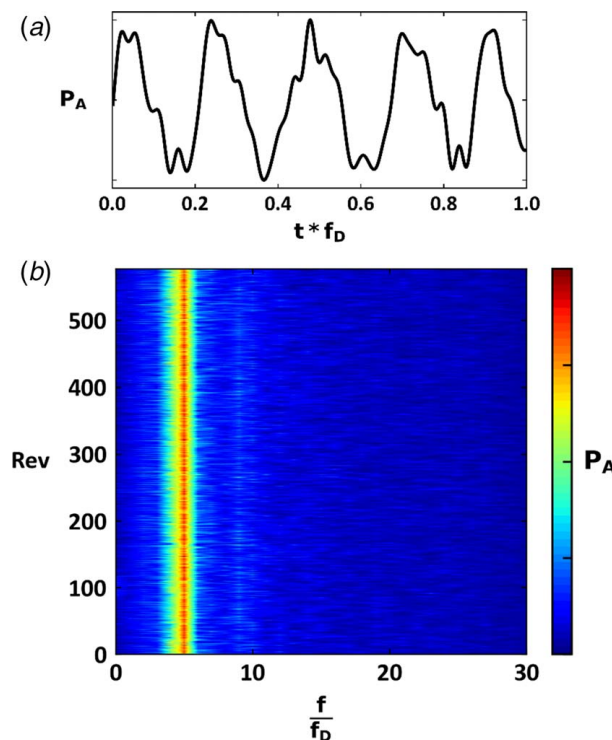


Fig. 7 Pressure signal P_A shown as a function of (a) time and (b) time and frequency. Note that the time axis in (b) is presented as revolutions.

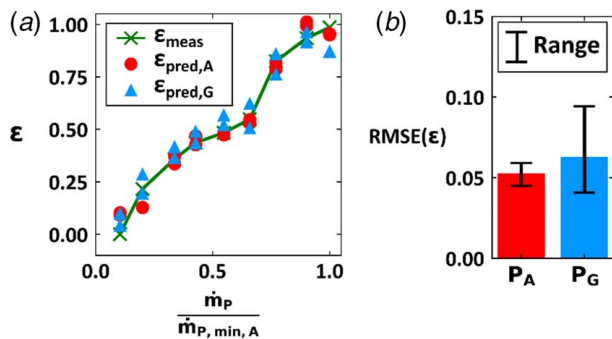


Fig. 8 DD model performance results for sensors P_A and P_G , showing (a) prediction comparison to measurements and (b) RMSE(ϵ) across all 250 grouping repetitions

allows the pressure fluctuations associated with the fluid dynamics in the rim seal region to be measured with less attenuation. However, the partial attenuation of the rim seal pressure fluctuations did not prohibit the development of a model that used sensor P_G to predict rim sealing effectiveness.

Based on the preference for FFT predictions shown in Fig. 6, the relative performance of predictions from measurements at locations A and G are compared in Fig. 8. Figure 8(a) shows the predicted sealing effectiveness from each sensor across a range of flowrates using both sensors, and the FFT results from Fig. 6 are isolated in Fig. 8(b). Specifically, Fig. 8(a) shows the predictions corresponding to the median RMSE(ϵ), which is shown by the bar height in Fig. 8(b).

Figure 8(a) shows the ability of the model to resolve the local characteristics of the sealing effectiveness curve, and Fig. 8(b) emphasizes the superior performance of sensor P_A relative to sensor P_G . Critically, the inflection region, located in the range $0.4 < \dot{m}_P / \dot{m}_{P, \min, A} \leq 0.7$, is captured well by both predictions from both sensor locations. However, near the purge flow extrema, the predictions are not well centered on the sealing effectiveness measurements. This characteristic is important because engines are typically designed to operate at or close to fully sealed conditions [22]. With this range in mind, some statements can be made about the applicability of the observed prediction accuracy.

There are two primary goals for implementing a diagnostic model: fault diagnosis and health monitoring. Fault diagnosis is the less stringent of the two goals because it only requires the detection of sealing effectiveness that has dropped below some critical value. If that critical sealing effectiveness were set to the minimum of the design range, then an RMSE(ϵ) of about 0.05 or 0.06 (as shown in Fig. 8(b)) would be sufficient to identify when the sealing effectiveness drops below the critical value. However, accuracies shown in Fig. 8 are likely insufficient to provide distinct sealing effectiveness predictions within the design range. This issue is central to the goal of health monitoring, which strives to relate the cumulative time history of sealing effectiveness predictions to the health of the under-platform components. Therefore, the sealing effectiveness prediction error must be further minimized to improve health monitoring accuracy.

Two-Step Modeling With Domain Knowledge

The DD modeling approach presented in the previous section was naive in its approach by neglecting to account for any physical understanding of the relationship between the pressure signal and the rim sealing effectiveness. As confirmed in the study by Siroka et al. [32], the presence and the strength of the rotating flow structures in the under-platform region significantly influences the sealing effectiveness. While the DD modeling approach was successful, it is likely that leveraging the specific frequency or

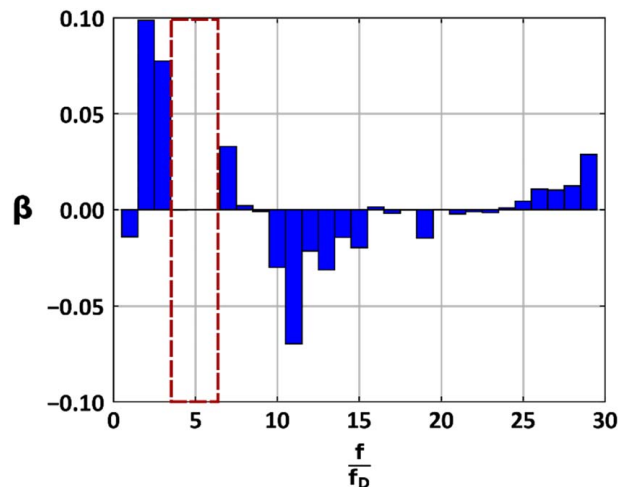


Fig. 9 Model coefficients from the LASSO regression, which relate the grouped spectral features of the pressure signal to the sealing effectiveness. The dashed box indicates the approximate frequency range associated with the dominant frequency.

frequencies corresponding to the rotating flow structures could result in lower prediction error.

To examine how the DD model utilized the dominant frequency corresponding to these rotating flow structures, the model coefficients (β) were examined, as shown in Fig. 9. The coefficient values from all 250 modeling iterations were averaged to yield a single representative coefficient value for each frequency bin (feature). The magnitude of each coefficient indicates the relative degree to which the pressure amplitude is correlated with the sealing effectiveness. Here, the various forms of the term “correlation” are used in accordance with their statistical definition, which is a measure of the interdependency between two variables. Most notably, the coefficients corresponding to the dominant frequency, typically in the range $3.5 < f / f_D < 6.5$, are nearly zero, which shows that the dominant frequency was not used. Therefore, a two-step (2S) modeling approach was developed to investigate a potential added benefit of utilizing the dominant frequency. This new methodology employs an understanding of the fluid dynamics to create a better model—an approach commonly referred to as the inclusion of “domain knowledge.”

As shown in Fig. 4, the trend of dominant frequency amplitude represents a nonmonotonic relationship with purge flow. Based on this relationship, the use of the dominant frequency amplitude on its own yields a nonunique solution for sealing effectiveness. To address this limitation, the 2S modeling approach applies one model where the sealing effectiveness and amplitude of the dominant frequency are positively correlated and applies a second model where the sealing effectiveness and amplitude of the dominant frequency are negatively correlated. By separating the data in this way, linear regression is able to relate the pressure features to the sealing effectiveness.

The 2S model diagram is shown in Fig. 10. The first three boxes of the 2S model are identical to the DD model. FFT was used as the feature extraction method because of its superior performance shown with the DD model. The upper and lower paths of the model diagram denote the training and testing procedures, respectively. Within these paths, the two steps that differentiate the 2S approach from the DD approach were implemented.

The first step of the 2S approach utilizes a binary regime model to identify the sealing effectiveness within either the increasing or decreasing regions of the sealing effectiveness curve. This step is nearly identical to the DD model through its use of all spectral features to predict sealing effectiveness. However, instead of performing LASSO regression to obtain a continuous prediction of sealing effectiveness, the binary regime model uses logistic regression to

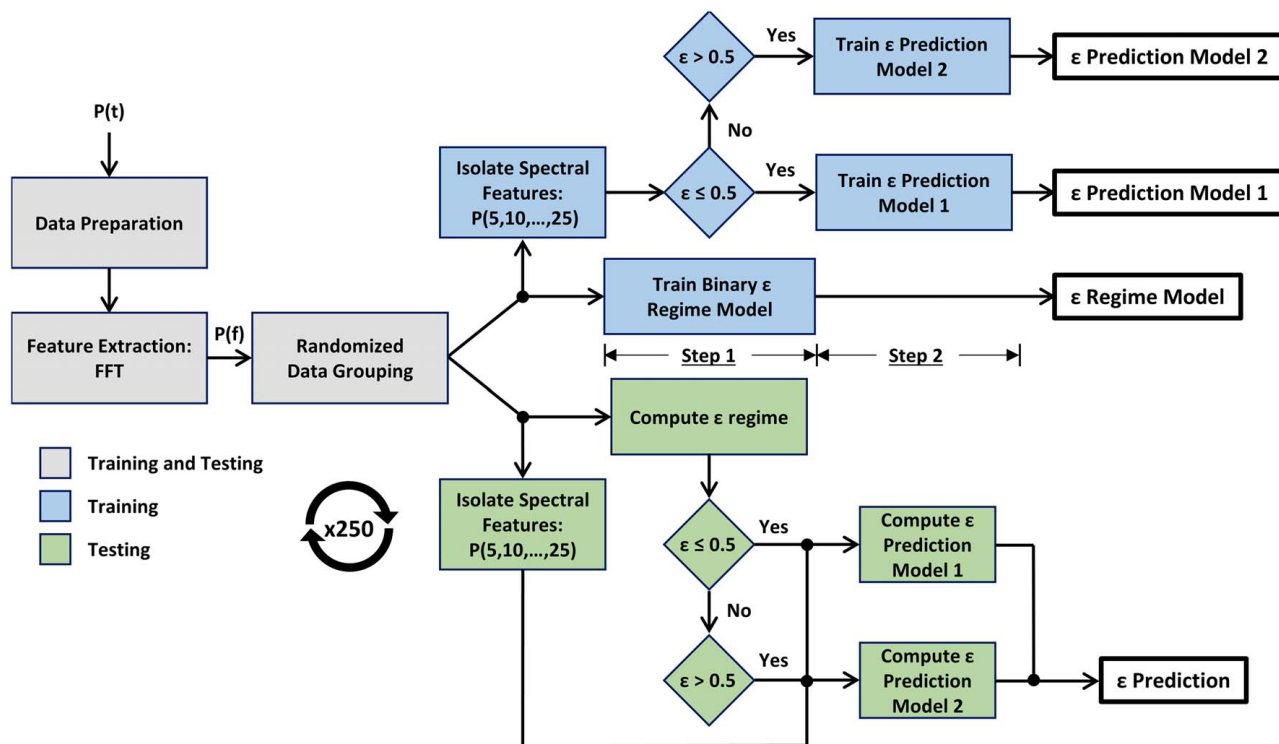


Fig. 10 Two-step (2S) modeling diagram

obtain an output corresponding to the sealing effectiveness regime relative to a sealing effectiveness value of 0.5 (as dictated by trends in Fig. 4).

The second step of the 2S approach implements an additional grouping to isolate a subset of features corresponding to the large-scale rotating structures and associated harmonics ($f/f_D = 5, 10, \dots, 25$). The isolated features, along with their logarithm transforms, were sorted based upon their measured sealing effectiveness regime (greater or less than 0.5), and then LASSO regression was used to create the sealing effectiveness prediction models. Model performance was evaluated with and without the logarithm contributors. Although 2S improvements relative to DD were identified both with and without logarithms, the addition of relevant feature logarithms helped capture the inherent nonlinearity of the dominant frequency amplitude trend (Fig. 4), which resulted in additional 2S model benefits.

In total, three models were trained for 2S implementation—one ϵ regime model and two ϵ prediction models, as shown in the black boxes in the top right of Fig. 10. During the 2S model testing phase, the binary ϵ regime model predicts the approximate range of the sealing effectiveness, which then informs the prediction model to apply to acquire a final sealing effectiveness prediction.

The accuracies of the DD and 2S model predictions are compared in Fig. 11. The predictions shown in Figs. 11(a) and 11(b) correspond to the median RMSE(ϵ) data grouping iteration predictions. In Fig. 11(c), the bar height corresponds to the median RMSE(ϵ) and the range bars indicate the variation in RMSE(ϵ) across 250 grouping repetitions, excluding outliers. Overall, Fig. 11(c) shows the 2S modeling approach reduced RMSE(ϵ) by 48% at location A and 37% at location G relative to the DD approach. Furthermore, Fig. 11(c) supports the previous conclusion that P_A predictions are superior to P_G predictions. The accuracy improvement of the 2S model is most notable at the highest purge flowrates, as indicated in Figs. 11(a) and 11(b).

To investigate this relationship between purge flowrate and model performance in greater detail, Fig. 12 shows RMSE(ϵ) as a function of purge flowrate. For the DD modeling approach, RMSE(ϵ) grows as the purge flowrate nears its maximum value for both sensors. However, the 2S modeling approach RMSE(ϵ)

does not suffer from this issue. Instead, the RMSE(ϵ) of the 2S approach is consistently low at high purge flowrates. Furthermore, when examining a single sensor, the 2S approach RMSE(ϵ) is typically lower than or equal to the RMSE(ϵ) of the DD approach across all purge flowrates.

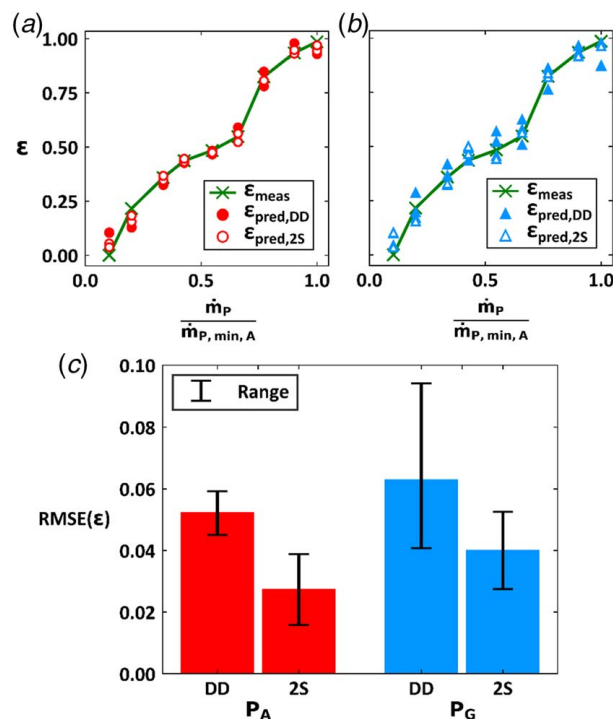


Fig. 11 DD and 2S model performance comparison of predictions relative to measurements for (a) sensor P_A and (b) sensor P_G , as well as (c) RMSE(ϵ) results across all 250 grouping repetitions

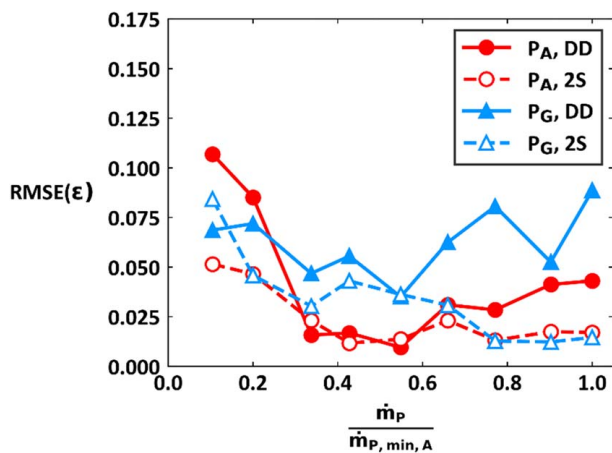


Fig. 12 Prediction error of DD and 2S modeling approaches as a function of purge flowrate

Based on knowledge that engines typically operate near the fully sealed condition, the low errors at high purge flowrates exhibited by the 2S approach is especially useful. As an example, if an engine were designed to operate with sealing effectiveness between 0.8 and 1.0 (the highest three purge flowrates studied), the 2S model RMSE(ϵ) is approximately one order of magnitude less than the design intent sealing effectiveness range. As a result, the RMSE(ϵ) of the 2S modeling approach is likely sufficiently low to be implemented in a true health monitoring application. Furthermore, the prediction errors from sensor P_G , at the casing, are nearly equivalent to the prediction errors from sensor P_A , in the rim seal, which supports the viability of using sensor P_G for its easier installation access.

Practical Considerations

To this point, two modeling approaches have been presented to relate time-resolved rim seal pressure to rim sealing effectiveness. Both modeling approaches have shown the ability to predict sealing effectiveness with low error at one turbine operating point. However, it is important to consider the applicability of these models to other operating conditions and additional geometries, as well as to consider the practical aspects of training and implementing the models in a real-world scenario. The investigation of additional turbine operating points will primarily focus on the 2S modeling approach because of its superior performance.

Turbine monitoring models can be applied continuously at all operating points, or they can be applied at a subset of operating conditions. The former application requires full model flexibility at all operating points and returns monitored information continuously. The latter application can be valid only when the turbine operating conditions match the training conditions, which diminishes the monitoring frequency.

To examine the model sensitivity to turbine operating conditions, measurements were collected at a second turbine operating point (OP2). The relationship between the two sets of operating conditions is presented in Table 2 using the prime notation introduced in Table 1. Results at OP2 are shown for sensor P_G due to the

Table 2 OP2 operating conditions

Parameters	OP2
Inlet absolute total pressure, P'_{in}	0.9
Total pressure ratio, $(P'_{in}/P'_{out})'$	0.82
Mass flowrate, \dot{m}'_{MGP}	0.88
Rotating speed, RPM'	0.88
Inlet temperature, T'_{in}	1

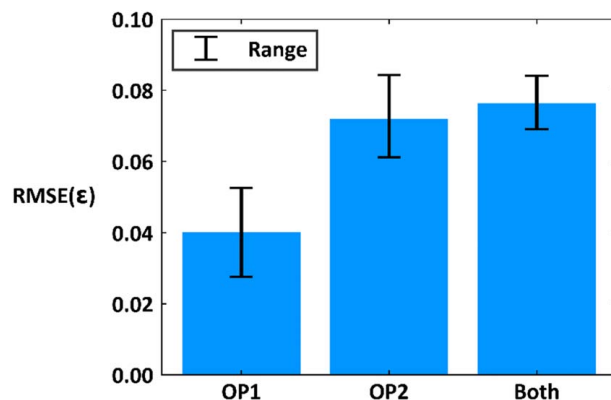


Fig. 13 Comparison of 2S model prediction error when trained individually at two operating points (OP1, OP2), and when trained on data combined from the two operating points. These results are shown exclusively for sensor P_G .

preferred installation accessibility and because location G represents an upper bound for error from which to examine model prediction sensitivities.

In Fig. 13, the OP1 and OP2 bars represent the median prediction RMSE(ϵ) when the 2S model is separately trained at OP1 and OP2, respectively. The comparison shows OP2 median error is nearly double the OP1 median error—an observation that could be caused by increased variability in the amplitude of the dominant frequency at a given sealing effectiveness for different turbine operating conditions.

The bar labeled “Both” represents the prediction error when a single model is generated based on the cumulative pressure and sealing effectiveness inputs from both operating conditions. The error of this combined model is nearly equivalent to the OP2 prediction error, which suggests the viability of applying a single model to a broad range of operating conditions. This observation also shows that the relationship between the standardized pressure amplitude of the dominant frequency and the sealing effectiveness is largely invariant across the range of evaluated operating conditions. These results indicate that the 2S model can be trained at two operating points with minimal losses in accuracy, which enables real-time rim sealing effectiveness monitoring at two operating points. While these results do not present a comprehensive view of the performance of a single model across all possible on and off-design operating conditions, Fig. 13 indicates capability of the modeling approach to function across a range of operating points, which supports continuous monitoring of rim sealing effectiveness.

Another important practical consideration for these data-driven models is their applicability to various turbine geometries. Although this question cannot be explicitly answered without testing alternate turbine geometries, some instructive statements can be made by examining the working principles of the models themselves. Foremost, the 2S model relies on an instability-driven dominant frequency that follows amplitude variations as a function of the sealing effectiveness. Many researchers with differing turbine geometries and purge flow injection methods have observed low-frequency peaks in the rim seal pressure that are also dependent on purge flowrate [14,24,25,27,32,37,38]. Although many of these studies do not present results at as many purge flowrates as the present study, it is assumed that the 2S model (Fig. 10) can be modified to accommodate each individual relationship between rim seal time-resolved pressure and sealing effectiveness by modifying the extent and number of regimes corresponding to each prediction model.

While many turbines fit into this category, there are likely many turbine geometries that either do not show a dominant frequency in the rim seal pressure or do not exhibit a modulation of the pressure spectral content by purge flowrate variation. For example, Julien et al. [15] showed minor changes to rim seal pressure content

using CFD, and Darby et al. [26] hypothesized that co-swirled purge flow weakens the shear layer driven instability that creates a dominant frequency in the rim seal pressure. In these cases when dominant frequency content is not present, the DD modeling approach can still be applied because it does not rely on the presence of a dominant frequency to predict sealing effectiveness, as shown in Fig. 9.

Another challenge of applying the 2S and DD modeling approaches to an engine is the extreme temperatures in the turbine, which many sensing technologies cannot accommodate. Furthermore, the models presented in this study specifically require a pressure sensor capable of resolving fast-response pressure data up to approximately $f/f_D = 30$. For large turbines typical of power generation applications, the rotating speeds are relatively low, meaning the required sensor bandwidth is reduced and is therefore increasingly attainable. For example, a sensor applied to a turbine operating at 3600 rpm would require a sampling rate of 3.6 kHz to resolve $f/f_D = 30 = 1.8$ kHz, which is a reasonable sampling rate considering the existing technology for engine applications. Based on higher bandwidth requirements of smaller engines used in aerospace applications, the modeling approaches presented in this study may be most readily applied to large power generation engines. However, new sensor technologies are continuing to be developed that address this need for higher sensor bandwidth in engines with higher operating speeds.

Finally, it is important to consider the environment in which these models are trained and the relevance of the resulting model to the engine environment. Ideally, a gas turbine manufacturer would execute the training procedure with a pressure sensor installed on the exact engine to which the model would be applied; however, this poses several challenges including independent control requirements of cooling flow supplies, separate quantification of sealing effectiveness, and temperature controls to prevent component failure at low purge flowrates. Instead, test facility experimentation and CFD predictions present two potential alternatives to the engine for generating training data. Critically, the training data must closely match the relationship between time-resolved rim seal pressure and rim sealing effectiveness in the engine. Although great progress has been made recently in predicting rim seal flow characteristics using CFD [58–60], the authors are not aware of any studies in the open literature that have shown exact, or nearly exact, matches between CFD predictions and experimental results for time-resolved rim seal pressure and rim sealing effectiveness. Therefore, in pursuit of the highest fidelity source of training data, it is likely that the model would need to be trained in a test facility using turbine geometry that matches the engine. Continued development and utilization of turbine research facilities operating with true-scale engine hardware and engine-relevant operating conditions will help ensure the feasibility of such ex situ training methods.

Conclusions

This study developed models to predict real-time turbine rim sealing effectiveness using input data from a time-resolved pressure sensor with relatively low-bandwidth requirements. Fast-response pressure measurements were gathered in a one-stage test turbine operating at engine-relevant conditions with engine-representative hardware. Two pressure sensors were installed to examine the trade-off between ease of installation and model performance. Because unsteady rim seal flows are not yet fully understood, data-driven modeling approaches were used to relate the pressure signals to the sealing effectiveness.

These efforts resulted in the generation of two data-driven modeling approaches relating broadband pressure features to measured rim sealing effectiveness: a purely data-driven approach and a more complex approach integrating domain knowledge from known turbine rim seal behaviors. The first data-driven approach showed median sealing effectiveness predictions within approximately 6% of the measured value. The second approach incorporated domain

knowledge using a two-step approach and reduced median prediction errors to approximately 3% of the measured sealing effectiveness. For engines designed to operate at sealing effectiveness values above 0.8, these errors were found to be further reduced to below 2%—low enough to reasonably apply the model to real-time under-platform hardware health monitoring.

A comparison of the two sensor mounting locations showed the rim seal pressure sensor resulted in more accurate sealing effectiveness predictions than the casing pressure sensor. However, slight increases of prediction accuracy identified for the casing sensor location are likely outweighed by the preferable sensor accessibility.

Performance of the two-step model with domain knowledge was further assessed for different turbine operating conditions. Successful model integration showed that it is possible to train a single model for a range of turbine operating conditions, and the associated performance debits were quantified. Ultimately, the results from this study show the viability of a real-time health monitoring system for accurate predictions of turbine rim sealing behavior using a data-driven approach.

Acknowledgment

This material is based upon work supported by the Department of Energy under Award Number DE-FE0031288. The authors would also like to recognize and thank Pratt & Whitney for supporting research presented in this article. This report was prepared as an account of work sponsored by an agency of the United States Government. Neither the United States Government nor any agency thereof, nor any of their employees, makes any warranty, express or implied, or assumes any legal liability or responsibility for the accuracy, completeness, or usefulness of any information, apparatus, product, or process disclosed, or represents that its use would not infringe privately owned rights. Reference herein to any specific commercial product, process, or service by trade name, trademark, manufacturer, or otherwise does not necessarily constitute or imply its endorsement, recommendation, or favoring by the United States Government or any agency thereof. The views and opinions of authors expressed herein do not necessarily state or reflect those of the United States Government or any agency thereof.

Conflict of Interest

There are no conflicts of interest.

Data Availability Statement

The authors attest that all data for this study are included in the paper.

Nomenclature

c	= CO ₂ concentration
f	= frequency
t	= time
P	= pressure
T	= temperature
\dot{m}	= mass flowrate
RMSE(ε)	= root-mean-square error of ε prediction
β	= model coefficient
ε	= sealing effectiveness
σ	= standard deviation

Subscripts

2S	= two-step modelling approach
A	= rim seal location

D = relating to the disk rotation
 DD = data-driven modelling approach
 G = casing location
 in = inlet parameter
 max = maximum value
 $meas$ = measured using gas concentration method
 MGP = pertaining to the main gas path
 min = minimum value
 out = outlet parameter
 P = pertaining to pressure or purge flow
 $pred$ = predicted quantity

Superscripts and Operators

Q' = nondimensionalized by operating point OPI
 Q^* = globally normalized across all data
 \bar{Q} = mean quantity
 \hat{Q} = standardized quantity

References

- [1] Bunker, R. S., 2017, "Evolution of Turbine Cooling," ASME Turbo Expo 2017, Charlotte, NC, Paper No. GT2017-63205.
- [2] Tahan, M., Tsoutsanis, E., Muhammad, M., and Abdul Karim, Z. A., 2017, "Performance-Based Health Monitoring, Diagnostics and Prognostics for Condition-Based Maintenance of Gas Turbines: A Review," *Appl. Energy*, **198**, pp. 122–144.
- [3] Urban, L., 1969, *Gas Turbine Engine Parameter Interrelationships*, HSD UTC, Windsor Locks, CT.
- [4] Johnson, B. V., Mack, G. J., Paolillo, R. E., and Daniels, W. A., 1994, "Turbine Rim Seal Gas Path Flow Ingestion Mechanisms," AIAA/ASME/SAE/ASEE Joint Propulsion Conference, Indianapolis, IN, Paper No. AIAA 94-2703.
- [5] Scobie, J. A., Sangan, C. M., Michael Owen, J., and Lock, G. D., 2016, "Review of Ingress in Gas Turbines," *ASME J. Eng. Gas Turbines Power*, **138**(12), p. 120801.
- [6] Clark, K., Barringer, M., Thole, K., Clum, C., Hiester, P., Memory, C., and Robak, C., 2016, "Using a Tracer Gas to Quantify Sealing Effectiveness for Engine Realistic Rim Seals," ASME Turbo Expo 2016, Seoul, South Korea, Paper No. GT2016-58095.
- [7] Denton, J. D., and USW, S., 1981, "Use of a Tracer Gas Technique to Study Mixing in a Low Speed Turbine," ASME Gas Turbine Conference and Products Show, Houston, TX, Paper No. 81-GT-86.
- [8] Sangan, C. M., Pountney, O. J., Zhou, K., Wilson, M., Owen, J. M., and Lock, G. D., 2013, "Experimental Measurements of Ingestion Through Turbine Rim Seals—Part I: Externally Induced Ingress," *ASME J. Turbomach.*, **135**(2), p. 021012.
- [9] Owen, J. M., 2011, "Prediction of Ingestion Through Turbine Rim Seals—Part I: Rotationally Induced Ingress," *ASME J. Turbomach.*, **133**(3), p. 031005.
- [10] Owen, J. M., 2011, "Prediction of Ingestion Through Turbine Rim Seals—Part II: Externally Induced and Combined Ingress," *ASME J. Turbomach.*, **133**(3), p. 031006.
- [11] Savov, S. S., and Atkins, N. R., 2017, "A Rim Seal Ingress Model Based on Turbulent Transport," ASME Turbo Expo 2017, Charlotte, NC, Paper No. GT2017-63531.
- [12] Bohn, D., Johann, E., and Kruger, U., 1995, "Experimental and Numerical Investigations of Aerodynamic Aspects of Hot Gas Ingestion in Rotor-Stator Systems With Superimposed Cooling Mass Flow," International Gas Turbine and Aeroengine Congress and Exposition, Houston, TX, Paper No. 95-GT-143.
- [13] Rabs, M., Benra, F. K., Dohmen, H. J., and Schneider, O., 2009, "Investigation of Flow Instabilities Near the Rim Cavity of a 1.5 Stage Gas Turbine," ASME Turbo Expo 2009, Orlando, FL, Paper No. GT2009-59965.
- [14] Horwood, J. T. M., Hualca, F. P., Wilson, M., Scobie, J. A., Sangan, C. M., Lock, G. D., Dahlqvist, J., and Fridh, J., 2020, "Flow Instabilities in Gas Turbine Chute Seals," *ASME J. Eng. Gas Turbines Power*, **142**(2), p. 021019.
- [15] Julien, S., Lefrançois, J., Dumas, G., Boutet-blais, G., Lapointe, S., Caron, J.-F., and Marini, R., 2010, "Simulations of Flow Ingestion and Related Structures in a Turbine Disk Cavity," ASME Turbo Expo 2010, Glasgow, UK, Paper No. GT2010-22729.
- [16] Johnson, B. V., Wang, C.-Z., and Roy, R. P., 2008, "A Rim Seal Orifice Model With Two Cd's and Effects of Swirl in Seals," ASME Turbo Expo, Berlin, Germany, Paper No. GT2008-50650.
- [17] Johnson, B. V., Jakoby, R., Bohn, D. E., and Cunat, D., 2009, "A Method for Estimating the Influence of Time-Dependent Vane and Blade Pressure Fields on Turbine Rim Seal Ingestion," *ASME J. Turbomach.*, **131**(2), p. 021005.
- [18] Hills, N. J., Chew, J. W., and Turner, A. B., 2002, "Computational and Mathematical Modeling of Turbine Rim Seal Ingestion," *ASME J. Turbomach.*, **124**(2), pp. 306–315.
- [19] Chew, J. W., Dadkhah, S., and Turner, A. B., 1992, "Rim Sealing of Rotor-Stator Wheelspaces in the Presence of External Flow," *ASME J. Turbomach.*, **114**(2), pp. 433–438.
- [20] Sangan, C. M., Pountney, O. J., Zhou, K., Owen, J. M., Wilson, M., and Lock, G. D., 2013, "Experimental Measurements of Ingestion Through Turbine Rim Seals—Part II: Rotationally Induced Ingress," *ASME J. Turbomach.*, **135**(2), p. 021013.
- [21] Owen, J. M., Wu, K., Scobie, J. A., Sangan, C. M., Cho, G., and Lock, G. D., 2015, "Use of Pressure Measurements to Determine Effectiveness of Turbine Rim Seals," *ASME J. Eng. Gas Turbines Power*, **137**(3), p. 032510.
- [22] Teuber, R., Li, Y. S., Maltson, J., Wilson, M., Lock, G. D., and Owen, J. M., 2013, "Computational Extrapolation of Turbine Sealing Effectiveness From Test Rig to Engine Conditions," *Proc. Inst. Mech. Eng., Part A: J. Power Energy*, **227**(2), pp. 167–178.
- [23] Gentilhomme, O., Hills, N. J., Turner, A. B., and Chew, J. W., 2003, "Measurement and Analysis of Ingestion Through a Turbine Rim Seal," *ASME J. Turbomach.*, **125**(3), pp. 505–512.
- [24] Hualca, F. P., Horwood, J. T. M., Sangan, C. M., Lock, G. D., and Scobie, J. A., 2020, "The Effect of Vanes and Blades on Ingress in Gas Turbines," *ASME J. Eng. Gas Turbines Power*, **142**(2), p. 021020.
- [25] Savov, S. S., Atkins, N. R., and Uchida, S., 2017, "A Comparison of Single and Double Lip Rim Seal Geometries," *ASME J. Eng. Gas Turbines Power*, **139**(11), p. 112601.
- [26] Darby, P. W., Mesny, A. W., De Cosmo, G., Carnevale, M., Lock, G., Scobie, J. A., and Sangan, C., 2020, "Conditioning of Leakage Flows in Gas Turbine Rotor-Stator Cavities," ASME Turbo Expo 2020, Virtual, Online, Paper No. GT2020-14308.
- [27] Horwood, J. T. M., Hualca, F. P., Wilson, M., Scobie, J. A., Sangan, C. M., and Lock, G. D., 2018, "Unsteady Computation of Ingress Through Turbine Rim Seals," ASME Turbo Expo 2018, Oslo, Norway, Paper No. GT2018-75321.
- [28] Patinios, M., Ong, I. L., Scobie, J. A., Lock, G. D., and Sangan, C. M., 2019, "Influence of Leakage Flows on Hot Gas Ingress," *ASME J. Eng. Gas Turbines Power*, **141**(2), p. 021010.
- [29] Balasubramanian, J., Pathak, P. S., Thiagarajan, J. K., Singh, P., Roy, R. P., and Mirzamohammad, A. V., 2015, "Experimental Study of Ingestion in the Rotor-Stator Disk Cavity of a Subscale Axial Turbine Stage," *ASME J. Turbomach.*, **137**(9), p. 091010.
- [30] Barringer, M. D., Coward, A., Clark, K. P., Thole, K. A., Schmitz, J., Wagner, J., Alvin, M. A., Burke, P., and Dennis, R., 2014, "The Design of a Steady Aero Thermal Research Turbine (START) for Studying Secondary Flow Leakages and Airfoil Heat Transfer," ASME Turbo Expo 2014, Dusseldorf, Germany, Paper No. GT2014-25570.
- [31] Berdianier, R. A., Monge-Concepción, I., Knisely, B. F., Barringer, M. D., Thole, K. A., and Grover, E. A., 2019, "Scaling Sealing Effectiveness in a Stator-Rotor Cavity for Differing Blade Spans," *ASME J. Turbomach.*, **141**(5), p. 051007.
- [32] Siroka, S., Monge-Concepción, I., Berdianier, R. A., Barringer, M., and Thole, K. A., 2021, "Correlating Cavity Sealing Effectiveness to Time-Resolved Rim Seal Events in the Presence of Vane Trailing Edge Flow," ASME Turbo Expo 2021, Virtual, Online, Paper No. GT2021-59285.
- [33] Figliola, R. S., and Beasley, D. E., 2014, *Theory and Design for Mechanical Measurements*, John Wiley & Sons, New York.
- [34] Monge-Concepción, I., Siroka, S., Berdianier, R. A., Barringer, M. D., Thole, K. A., and Robak, C., 2021, "Unsteady Turbine Rim Sealing and Vane Trailing Edge Flow Effects," ASME Turbo Expo 2021, Virtual, Online, GT2021-59273.
- [35] Bohn, D., Rudzinski, B., Sürken, N., and Gärtner, W., 1999, "Influence of Rim Seal Geometry on Hot Gas Ingestion Into the Upstream Cavity of an Axial Turbine Stage," International Gas Turbine & Aeroengine Congress & Exhibition, Indianapolis, IN, Paper No. 99-GT-248.
- [36] Bohn, D., Rudzinski, B., Sürken, N., and Gärtner, W., 2000, "Experimental and Numerical Investigation of the Influence of Rotor Blades on Hot Gas Ingestion Into the Upstream Cavity of an Axial Turbine Stage," Turbo Expo 2000, Munich, Germany, Paper No. 2000-GT-284.
- [37] Jakoby, R., Zierer, T., Lindblad, K., Larsson, J., DeVito, L., Bohn, D. E., Funcke, J., and Decker, A., 2004, "Numerical Simulation of the Unsteady Flow Field in an Axial Gas Turbine Rim Seal Configuration," ASME Turbo Expo 2004, Vienna, Austria, Paper No. GT2004-53829.
- [38] Wang, C.-Z., Mathiyalagan, S. P., Johnson, B. V., Glahn, J. A., and Cloud, D. F., 2014, "Rim Seal Ingestion in a Turbine Stage From 360 Degree Time-Dependent Numerical Simulations," *ASME J. Turbomach.*, **136**(3), p. 031007.
- [39] Cao, C., Chew, J. W., Millington, P. R., and Hogg, S. I., 2004, "Interaction of Rim Seal and Annulus Flows in an Axial Flow Turbine," *ASME J. Eng. Gas Turbines Power*, **126**(4), pp. 786–793.
- [40] Beard, P. F., Gao, F., Chana, K. S., and Chew, J., 2017, "Unsteady Flow Phenomena in Turbine Rim Seals," *ASME J. Eng. Gas Turbines Power*, **139**(3), p. 032501.
- [41] Boudet, J., Hills, N. J., and Chew, J. W., 2006, "Numerical Simulation of the Flow Interaction Between Turbine Main Annulus and Disc Cavities," ASME Turbo Expo, Barcelona, Spain, Paper No. GT2006-90307.
- [42] Chilla, M., Hodson, H., and Newman, D., 2013, "Unsteady Interaction Between Annulus and Turbine Rim Seal Flows," *ASME J. Turbomach.*, **135**(5), p. 051024.
- [43] de la Rosa Blanco, E., Hodson, H. P., and Vazquez, R., 2009, "Effect of the Leakage Flows and the Upstream Platform Geometry on the Endwall Flows of a Turbine Cascade," *ASME J. Turbomach.*, **131**(1), p. 011004.
- [44] Laskowski, G. M., Bunker, R. S., Bailey, J. C., Ledezma, G., Kapetanovic, S., Itzel, G. M., Sullivan, M. A., and Farrell, T. R., 2011, "An Investigation of Turbine Wheel-space Cooling Flow Interactions With a Transonic Hot Gas Path—Part II: CFD Simulations," *ASME J. Turbomach.*, **133**(4), p. 041020.
- [45] Gao, F., Chew, J. W., Beard, P. F., Amirante, D., and Hills, N. J., "Numerical Studies of Turbine Rim Sealing Flows on a Chute Seal Configuration," 12th

- European Conference on Turbomachinery Fluid Dynamics and Thermodynamics, Paper No. ETC2017-284.
- [46] Town, J., Averbach, M., and Camci, C., 2016, "Experimental and Numerical Investigation of Unsteady Structures Within the Rim Seal Cavity in the Presence of Purge Mass Flow," ASME Turbo Expo 2016, Seoul, South Korea, Paper No. GT2016-56500.
- [47] Schädler, R., Kalfas, A. I., Abhari, R. S., Schmid, G., and Voelker, S., 2017, "Modulation and Radial Migration of Turbine Hub Cavity Modes by the Rim Seal Purge Flow," *ASME J. Turbomach.*, **139**(1), p. 011011.
- [48] Schuepbach, P., Abhari, R. S., Rose, M. G., Germain, T., Raab, I., and Gier, J., 2010, "Effects of Suction and Injection Purge-Flow on the Secondary Flow Structures of a High-Work Turbine," *ASME J. Turbomach.*, **132**(2), p. 021021.
- [49] Wang, X., Liao, G., Zhang, F., and Li, J., 2016, "Numerical Investigation on the Steady and Unsteady Flow Characteristics of Rim Seal for the First Stage in Gas Turbine," *Appl. Therm. Eng.*, **99**, pp. 11–22.
- [50] O'Mahoney, T. S. D., Hills, N. J., Chew, J. W., and Scanlon, T., 2011, "Large-Eddy Simulation of Rim Seal Ingestion," *Proc. Inst. Mech. Eng. J. Mech. Eng. Sci.*, **225**(12), pp. 2881–2891.
- [51] Gao, F., Poujol, N., Chew, J. W., and Beard, P. F., 2018, "Advanced Numerical Simulation of Turbine Rim Seal Flows and Consideration for RANS Turbulence Modelling," ASME Turbo Expo 2018, Oslo, Norway, Paper No. GT2018-75116.
- [52] Gao, F., Chew, J. W., and Marxen, O., 2020, "Inertial Waves in Turbine Rim Seal Flows," *Phys. Rev. Fluids*, **5**(2), p. 024802.
- [53] Pogorelov, A., Meinke, M., and Schröder, W., 2019, "Large-Eddy Simulation of the Unsteady Full 3D Rim Seal Flow in a One-Stage Axial-Flow Turbine," *Flow, Turbul. Combust.*, **102**(1), pp. 189–220.
- [54] Zhang, Z., Zhang, Y., Dong, X., Qu, X., Lu, X., and Zhang, Y., 2020, "Flow Mechanism Between Purge Flow and Mainstream in Different Turbine Rim Seal Configurations," *Chinese J. Aeronaut.*, **33**(8), pp. 2162–2175.
- [55] Boutet-blais, G., Lefrançois, J., Dumas, G., Julien, S., Harvey, J.-F., Marini, R., and Caron, J.-F., 2011, "Passive Tracer Validity for Cooling Effectiveness Through Flow Computation in a Turbine Rim Seal Environment," ASME Turbo Expo 2011, Vancouver, BC, Canada, Paper No. GT2011-45654.
- [56] Aretakis, N., and Mathioudakis, K., 1997, "Wavelet Analysis for Gas Turbine Fault Diagnostics," *ASME J. Eng. Gas Turbines Power*, **119**(4), pp. 870–876.
- [57] Tibshirani, R., 1996, "Regression Shrinkage and Selection Via the Lasso," *J. R. Stat. Soc. Ser. B*, **58**(1), pp. 267–288.
- [58] Palermo, D. M., Gao, F., Amirante, D., Chew, J. W., Bru Revert, A., and Beard, P. F., 2021, "Wall-Modelled Large Eddy Simulations of Axial Turbine Rim Sealing," *ASME J. Eng. Gas Turbines Power*, **143**(6), p. 061025.
- [59] Gao, F., Chew, J. W., Beard, P. F., Amirante, D., and Hills, N. J., 2018, "Large-Eddy Simulation of Unsteady Turbine Rim Sealing Flows," *Int. J. Heat Fluid Flow*, **70**, pp. 160–170.
- [60] Valencia, A. G., Dixon, J. A., Da Soghe, R., Facchini, B., Smith, P. E. J., Muñoz, J., Eastwood, D., Long, C. A., Coren, D. D., and Atkins, N. R., 2012, "An Investigation Into Numerical Analysis Alternatives for Predicting Re-Ingestion in Turbine Disc Rim Cavities," ASME Turbo Expo 2012, Copenhagen, Denmark, Paper No. GT2012-68592.